nature physics

SUPPLEMENTARY INFORMATION

DOI: 10.1038/NPHYS2543

Nanoscale magnetic imaging of a single electron spin under ambient conditions

Supplementary figures:

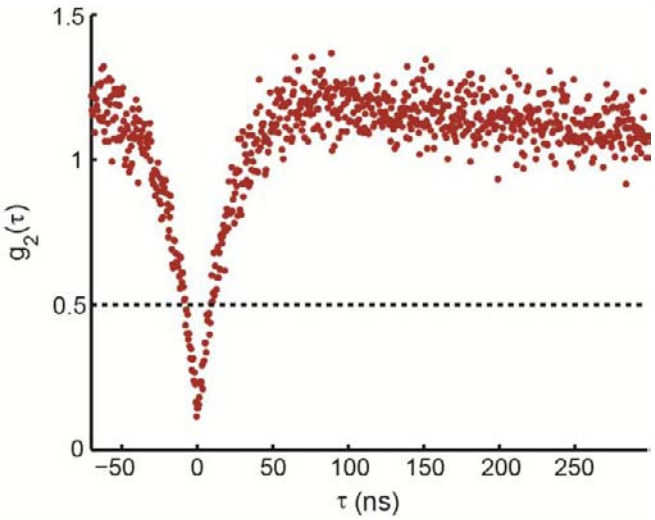


Figure S1: Photon-autocorrelation measurements for the target NV center

Photon-autocorrelation measurements for the target NV (in the absence of the sensor NV) give $g_2(\tau=0) < 0.5$, ensuring that a single target NV spin lies in the diamond mesa on which magnetic field imaging is performed with the scanning NV magnetometer. No background subtraction was performed on the data and normalization was performed based on count-rates on the individual detectors as well as the time-binning in the photon-correlation hardware.

DOI: 10.1038/NPHYS2543

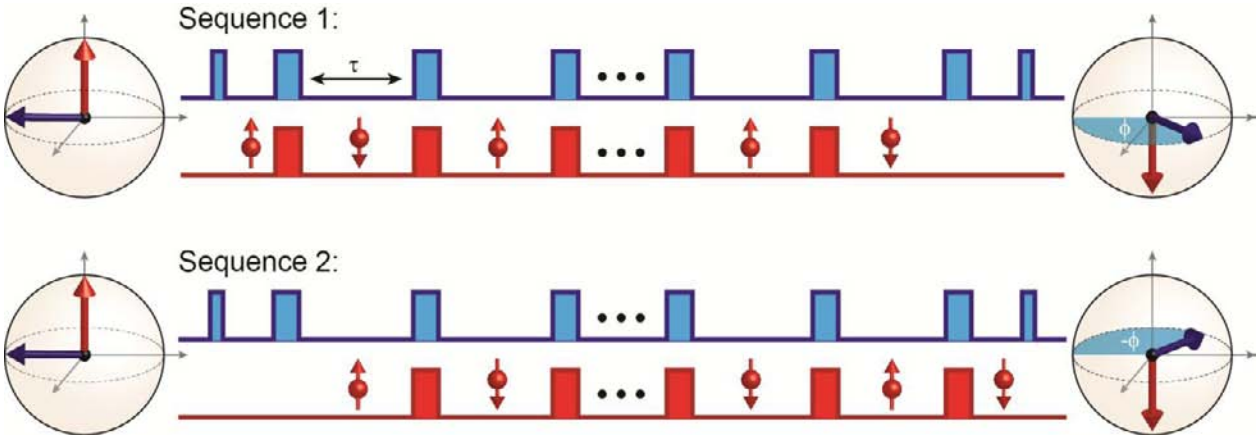


Figure S2: Magnetometry normalization scheme

To isolate the sensor NV's spin-state-dependent fluorescence from spatially varying background fluorescence, we employ a normalization scheme that involves alternatively performing two slightly different magnetometry pulse sequences, and then subtracting the measured NV fluorescence rates. These two sequences are similar to the double-electron-electron resonance scheme presented in Fig. 3, except that one target NV spin-inversion (performed via an adiabatic fast passage) is removed from each sequence: in Sequence 1, the last spin inversion is removed, while in Sequence 2 it is the first spin inversion. By removing spin inversions in this manner, we ensure that the sensor NV (blue arrow) acquires an equal and opposite target-spin-induced phase shift (ϕ, shaded blue region) during the two pulse sequences, because the target spin-state is inverted in the two sequences for the majority of the phase evolution time. Crucially, the target NV spin ends in the same state for the two pulse sequences (here, $|-1\rangle$). Thus subtracting the measured NV fluorescence rates for the two pulse sequences removes the contribution of background fluorescence from the NV target, which has a non-trivial spatial dependence (Fig. 2 of the main text). Moreover, both pulse sequences have the same number of target spin inversions, which alleviates unavoidable spin-polarization losses associated with flipping the target spin and cross-talk between the applied MW sources. In this scheme, a small amount of integration time is unused for sensor NV phase accumulation (the portions next to the $\pi/2$ pulses at the beginning and end of each sequence cancel, equal to one delay period τ between π pulses). However in the limit of a large number of spin inversions, this loss of integration time is negligible.

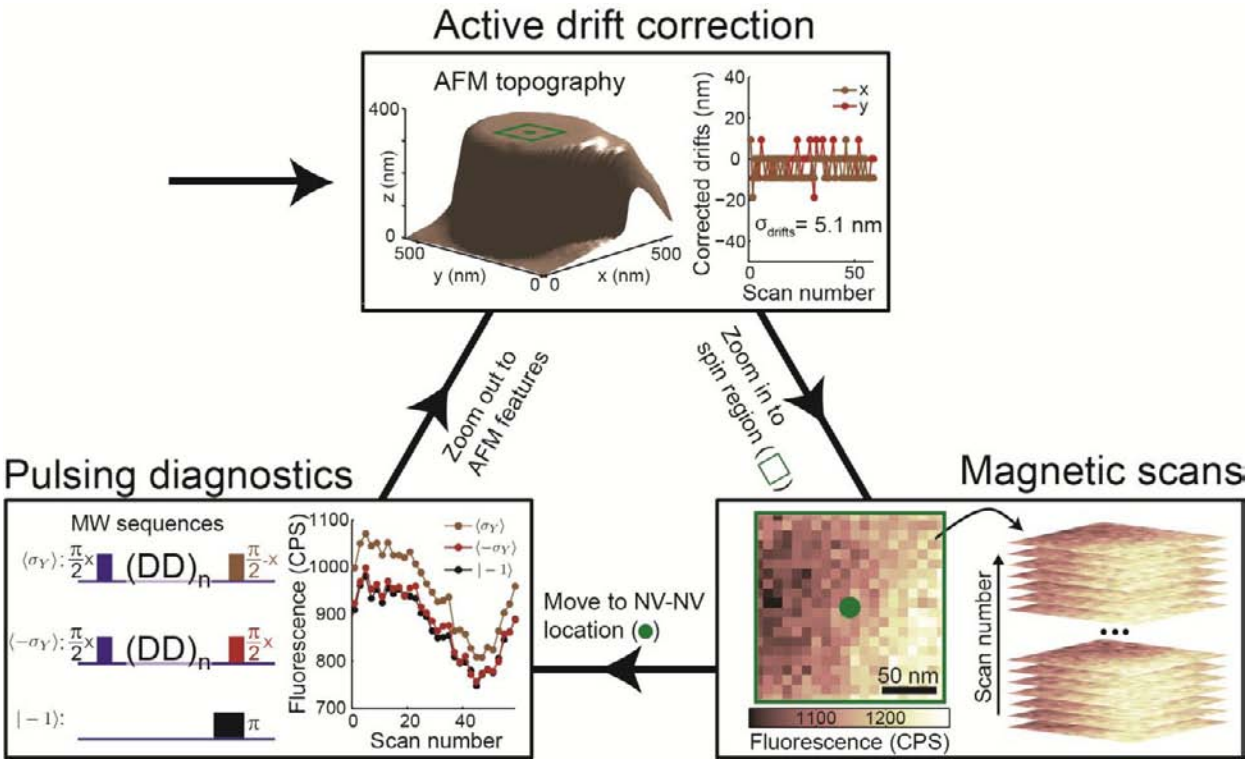


Figure S3: Magnetic field image acquisition protocol

Scanning an AFM for long periods of time with nanometer precision can be difficult to achieve under ambient conditions because of thermal-induced drifts. Temperature fluctuations on the order of a fraction of a degree can lead to tens of nanometers of relative motion between the sensor and target NV spins, which would considerably smear out our magnetic field imaging. These drifts generally occur on long time-scales, with a few nanometers of drift every hour. To minimize their effect, we employ an image acquisition protocol that periodically corrects for sensor-to-target drifts.

The protocol has three major components: (1) Drift-correction using the sample topography to determine the target's location (top panel); (2) Taking a relatively quick magnetic scan over the target spin location (lower right panel); and (3) Checking to make sure that the MW pulsing has not degraded over time, and that the sensor NV's magnetic sensitivity has not been significantly compromised (lower left panel).

Drift correction is performed by scanning over the target-containing diamond mesa, and the measured topography is the convolution of this mesa (~200 nm in diameter) with the diamond nanopillar scanning tip (~200 nm in diameter). From this topography, and the simultaneously measured fluorescence (as in Fig. 2 of the main text), the target NV spin can be located (green dot) and an appropriate scan range can be defined (green square). The topography of successive scans (taken after both magnetometry and diagnostic measurements), can be compared to the first reference scan by cross-correlation, and thus drifts can be corrected between scans. In the single-spin measurements presented in Fig. 4 of the main text, we observe a mean variation of 5 nm between successive scans (limited by the pixel size of the reference scan), indicating that magnetic field images can be overlapped with roughly 5-nm precision.

After zooming into the appropriate scan region, where the expected target spin NV lies in the center of the scan range, magnetic field images are acquired while simultaneously alternating between the two magnetic detection pulse sequences (Fig. S2) and monitoring their fluorescence rates (only one sequence is illustrated). Each scan is integrated for roughly 30 minutes to minimize the drifts between scans.

When a magnetic scan is finished, the sensor NV is placed at the approximate measurement position to measure the optimal sensitivity to the target NV and as a function of time. In general, the sensor NV can slowly drift in and out of the green laser confocal spot, causing variations in the overall

DOI: 10.1038/NPHYS2543

detected NV fluorescence. Additionally, the power of the MW source can drift, which can decrease the performance of dynamic decoupling and magnetometry pulse sequences. Magnetic field sensitivity is experimentally determined by running the magnetometry sequence, with the phase of the last $\pi/2$ pulse set at $\pm\pi/2$ (red and brown data points, respectively) to measure the $\langle -\sigma_Y \rangle$ and $\langle \sigma_Y \rangle$ projections of the sensor NV. The difference between these measurements gives the contrast and counts of the sensor NV's magnetic response, and when combined with the phase accumulation time, determines the magnetic field sensitivity of the sensor NV. To differentiate overall NV fluorescence rate changes from pulsing performance changes, we also measure fluorescence counts for the $|-1\rangle$ state (black data points), which should overlap with the $\langle -\sigma_Y \rangle$ measurement in the case of no pulse errors or dephasing.

After these pulse diagnostics, we zoom out to measure the topography of the sample again, completing a measurement cycle. This procedure is repeated until a desired signal-to-noise in the magnetic field image has been achieved.

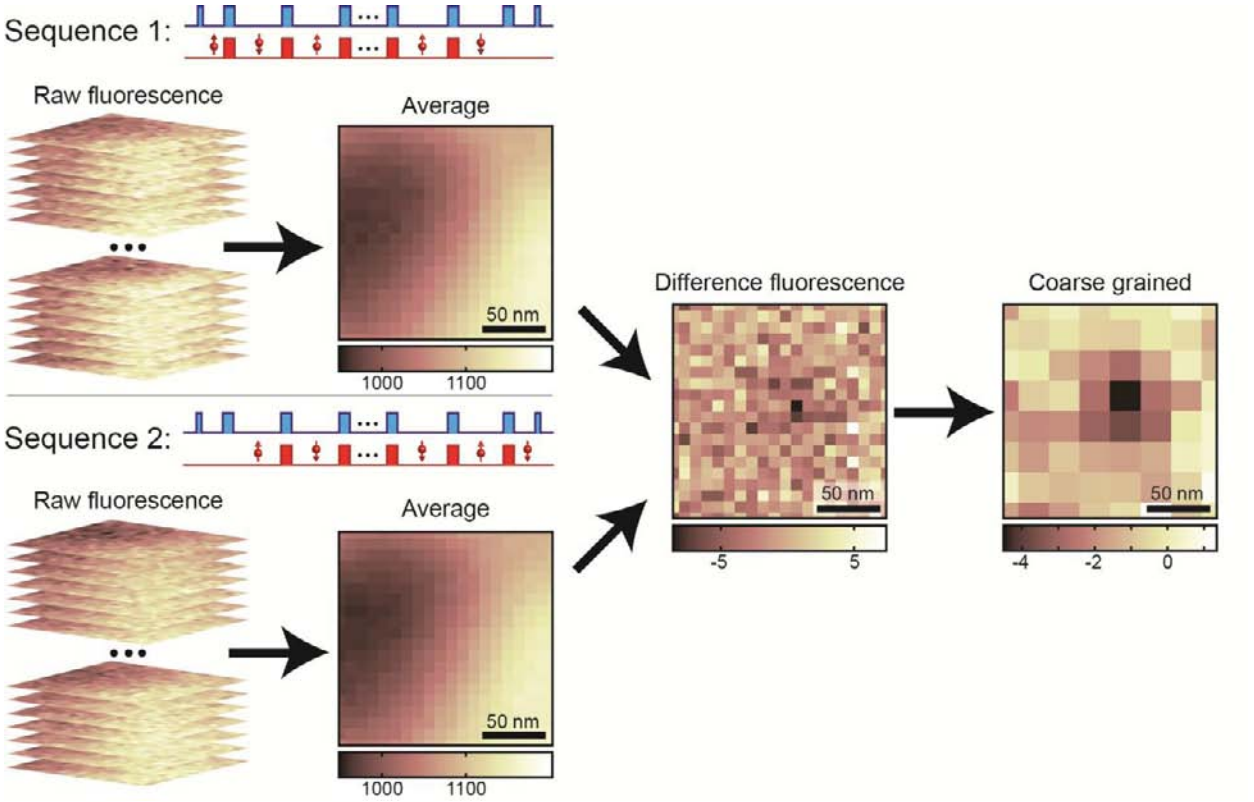
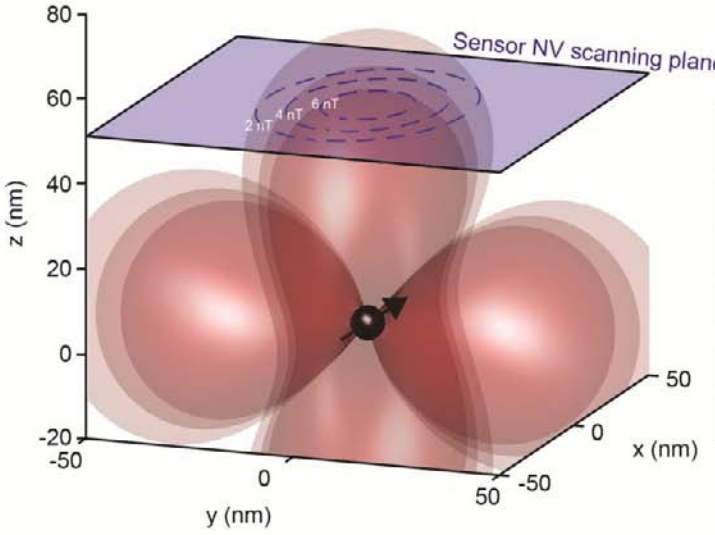


Figure S4: Magnetic field image data processing

The multiple images taken during a magnetic field scan for each magnetometry sequence (left column) are averaged (without any further spatial correction), to yield the average fluorescence map (center left column). In these averaged measurements, there are large variations in fluorescence due to near field coupling into and out of the diamond nanopillar for the target and sensor NV centers, as described in Fig. 2 of the main text. These variations are quite large (~150 CPS) compared to the expected effect of a single target NV's magnetic field on the sensor NV signal (fluorescence change ~4 CPS under inversion of the target NV spin). Subtracting the average fluorescence maps of the two magnetometry sequences yields a difference fluorescence signal free of the large background fluorescence (center right). In general, the difference in fluorescence between the two magnetometry sequences has a small remaining offset, and so it has a mean of a few counts per second, even in the absence of the target NV. This is likely due to a small amount of cross-talk between the target-addressing MW and the sensor NV, which is slightly different between the two sequences. During our pulsing diagnostics in the measurement acquisition, we measure this fluorescence offset with the sensor NV very far from the sample (>1 μm), and we subtract this value from the difference fluorescence, which yields a mean of zero counts per second away from the target NV spin. As long as this remainder fluorescence (4.3 CPS for this image) times the percent fluorescence variations across the scan region (15%) is smaller than the target NV spin signal — as is the case here — then the target NV spin signal will be the largest feature in the difference fluorescence map. To increase the signal-to-noise ratio (SNR) of magnetic field imaging, we average multiple pixels together to coarse-grain the scan (right panel), yielding a scan with 64 pixels across a field-of-view of ~200x200 nm, with 42 minutes of integration time per pixel providing average SNR of 4.3.

DOI: 10.1038/NPHYS2543



Measurement parameters	
Sensor NV axis	$[x,y,z] = \frac{1}{\sqrt{3}}[0,\sqrt{2},1]$
Target NV axis	$[x,y,z] = \frac{1}{\sqrt{3}}[0,-\sqrt{2},1]$
Sensor fluorescence	250 kCPS
Sensor contrast	6.5%
Evolution τ	40 μs

Figure S5: Simulation of single-spin magnetic field imaging

The response of the scanning NV magnetometer to a single electronic spin is simulated by considering the magnetic dipole field **B** from an electron spin:

$$\mathbf{B} = \frac{\mu_0}{4\pi}\left(\frac{3\mathbf{r}(\mathbf{m}\cdot\mathbf{r})}{r^5} - \frac{\mathbf{m}}{r^3}\right)$$

where μ_0 is the permeability of free space, and **r** is the displacement from the target spin, which lies at the origin. The magnetization of the target spin **m** has a magnitude one of Bohr magneton and is orientated along the [x,y,z] = $1/\sqrt{3}$ [0, $-\sqrt{2}$,1] direction (to match the target NV quantization axis in the sample that is measured through ESR measurements using a three-axis Helmholtz coils). Equi-field contours of this target spin's magnetic field are plotted as a function of three-dimensional space (displayed here are 2 nT, 4 nT, and 6 nT). Because the sensor NV is first-order sensitive only to magnetic fields along its quantization axis ([x,y,z] = $1/\sqrt{3}$ [0,$\sqrt{2}$,1]), the plotted field contours from the target spin have been projected along the sensor NV quantization axis, which yields the dipole field lobe pattern shown here. Experimental magnetic field scans are taken as plane-cuts of this dipole field pattern above the location of the target spin (at an a-priori unknown distance; plotted is the best fit value of 51 nm). The simulated magnetic field profile is converted into a spatial map of sensor NV fluorescence rate using the phase evolution time τ and the sensor NV's spin-based fluorescence (i.e. the difference in fluorescence between the m_S=0 and m_S=-1 states during a magnetometry sequence as measured in the pulsing diagnostic section in Fig. S3). This gives a magnetic field conversion factor of -1.8 nT per difference count per second. We note that this conversion factor depends on the collection efficiency of the sensor NV, and thus in our experiments depends on position as sensor fluorescence is quenched into the target diamond mesa. This quenching results in a roughly 13% variation in sensor NV counts across the scanned region (Fig. 2), and as such the conversion factor may vary by up to this amount in our magnetometry scans. We note, however, that the used conversion factor is calibrated at the location with the strongest signal, and its variations are smaller than the noise-to-signal ratio of our measurements, and so do not noticeably modify the conversion between magnetic field and difference fluorescence.

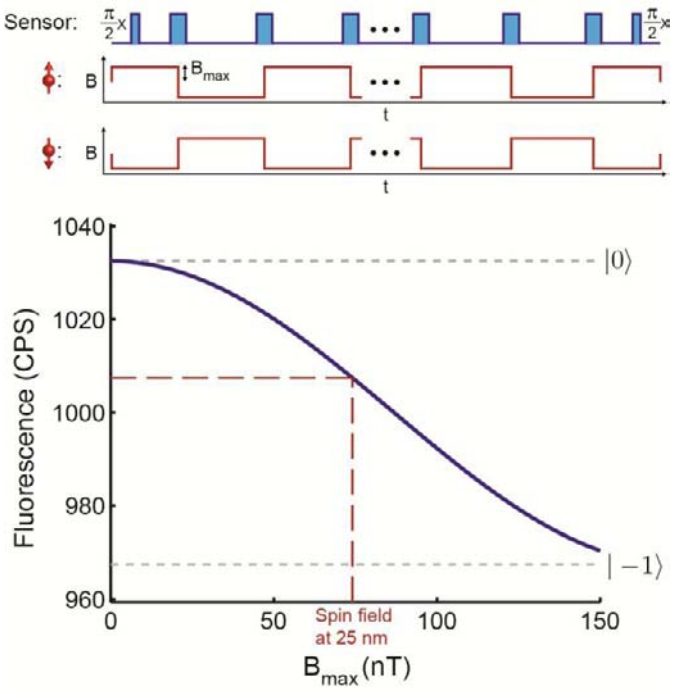


Figure S6: Simulation of measuring the variance of a non-initialized spin

If target electron spins cannot be initialized (unlike the target NV spin measured in this work), then the spin's magnetic field will average out to zero over multiple measurements, as at the start of a given measurement ("shot") the target spin has an equal probability of being either up or down. However, if the target's spin's longitudinal relaxation time is much longer than the magnetometry phase-evolution time τ, within a single shot, then the target spin maintains its statistical polarization, and a net phase shift will be accumulated by the sensor spin. By choosing the axis of rotation of the final $\pi/2$ pulse to match the axis of the first $\pi/2$ pulse, when the accumulated phase shifts from multiple measurement shots are converted to a net population difference, the effect of the target spin's magnetic field no longer cancels out and can be measured via the sensor NV's spin-dependent fluorescence. This scheme effectively measures the variance of the target spin polarization ($\langle\sigma_Z^2\rangle - \langle\sigma_Z\rangle^2$, for the thermal state of a target spin) instead of its mean polarization ($\langle\sigma_Z\rangle$)

Plotted here is the sensor NV's response for τ = 100 μs, plotted is the sensor's NV response to a (driven) target electron spin with random polarization (either up or down) at the measurement's start. (The sensor NV's fluorescence and spin-dependent contrast used are those demonstrated in spin-imaging; Supplementary Fig. 5.). The magnetic field profile for this driven target spin is a square wave with amplitude B_{max}, which is synchronized to the sensor NV's decoupling scheme. For a sensor-to-target distance of 25 nm (and the same sensor and target spin-quantization axes used in the present work; Supplementary Fig. 5), B_{max} = 74 nT, which gives a signal of 25 CPS with respect to the |0> state. Within two seconds of integration time, this signal divided by the measurement's shot noise gives a signal to noise ratio of one.

DOI: 10.1038/NPHYS2543

Supplementary discussion:

Dynamic decoupling of the sensor NV spin:

The sensor NV spin coherence time is prolonged by dynamically decoupling it from its noisy environment[1-3]. This is achieved by the repeated application of microwave (MW) π-pulses, which causes the effects of slowly fluctuating magnetic fields to re-phase and cancel out. To apply a large number of pulses without scrambling the sensor NV spin state, the control pulses are carefully calibrated to within 2% using a boot-strap tomography scheme[4]. For the dynamic decoupling scheme and magnetometry, we employ an XY8 sequence[5], which uses π-pulses around two orthogonal axes on the equator of the sensor NV's Bloch sphere to minimize the accumulation of pulse errors. This sequence (π_X - π_Y - π_X - π_Y - π_Y - π_X - π_Y - π_X) is repeated as many times as possible to maximize the sensor NV's magnetometry sensitivity, which — as a function of the number of pulses — is a compromise between the extended NV coherence from the decoupling and the reduced contrast from accumulated pulse errors.

MW fields are supplied from a Rhode and Schwarz SMB100A signal generator. MW phase control is achieved using an IQ mixer (Marki-1545) with pulsed analog inputs on the I and Q ports supplied by an arbitrary waveform generator (Tektronix AWG5000). NV spin Rabi frequencies in this work are 15-20 MHz, with typical π-pulse durations of 30 ns.

Adiabatic fast passages for controlling the target NV spin:

To control the target NV spin with high fidelity over numerous spin inversions, we employ adiabatic fast passages. The spin-state is prepared optically in the m_S = |0> state, and microwaves (MW) with bare Rabi frequency ω_R are applied and detuned by $\delta(t=0)$ from the target NV transition. The detuning is ramped through zero to $-\delta(t=0)$ over a pulse time, T_P. At any point in time, the target NV spin in the rotating frame prececess around an effective magnetic field Ω_R, which is the sum of the MW field and the remaining static magnetic field in

the rotating frame resulting from the non-zero MW detuning. If the angular velocity, $d\theta/dt$ of Ω_R is slow compared to ω_R, then the NV spin-state is effectively locked to the motion of this effective magnetic field as it moves from |0> to |–1>. To ensure that the passage is adiabatic throughout the applied pulse, we keep $d\theta/dt$ constant by applying the following time-dependent detuning:

$$\delta(t) = \omega_R \tan\left(\beta\left(\frac{t}{2T_P} - 1\right)\right)$$

where β is chosen to achieve the desired sweep range. For the adiabatic fast passages presented in Fig. 3 of the main text, T_P = 300 ns, δ(t=0) = 100 MHz, and ω_R = 17 MHz.

The detuning ramping is implemented by using an arbitrary waveform generator to output a sinusoid at a frequency of the desired detuning, which is mixed with a continuous-wave MW source (all are the same make and model as the sensor-addressing MW equipment). By setting the phase of this sinusoid to be the integral of the detuning as a function of time, the mixed MW frequency can be continuously varied.

1 de Lange, G., Ristè, D., Dobrovitski, V. V. & Hanson, R. Single-Spin Magnetometry with Multipulse Sensing Sequences. *Phys. Rev. Lett.* **106**, 080802 (2011).

2 de Lange, G., Wang, Z. H., Ristè, D., Dobrovitski, V. V. & Hanson, R. Universal Dynamical Decoupling of a Single Solid-State Spin from a Spin Bath. *Science* **330**, 60-63 (2010).

3 Bluhm, H. *et al.* Dephasing time of GaAs electron-spin qubits coupled to a nuclear bath exceeding 200[thinsp][mu]s. *Nature Phys.* **7**, 109-113 (2010).

4 Dobrovitski, V. V., de Lange, G., Ristè, D. & Hanson, R. Bootstrap Tomography of the Pulses for Quantum Control. *Phys. Rev. Lett.* **105**, 077601 (2010).

DOI: 10.1038/NPHYS2543

5 Gullion, T. & Schaefer, J. Elimination of resonance offset effects in rotational-echo, double-resonance NMR. *J. Magn. Reson.* **92**, 439-442 (1991).